

# Fluorescence-Detected Mid-Infrared Photothermal Microscopy

## Supporting information

Minghe Li<sup>1†</sup>, Aleksandr Razumtcev<sup>1†</sup>, Ruochen Yang<sup>2</sup>, Youlin Liu<sup>1</sup>, Jiayue Rong<sup>1</sup>, Andreas Geiger<sup>1</sup>, Romain Blanchard<sup>3</sup>, Cristian Pfluegl<sup>3</sup>, Lynne S. Taylor<sup>2</sup>, Garth J. Simpson<sup>1\*</sup>

<sup>1</sup>Department of Chemistry, Purdue University, West Lafayette IN, 47907. <sup>2</sup>Physical and Industrial Pharmacy, Purdue University, West Lafayette IN, 47907. <sup>3</sup>Pendar Technologies, 30 Spinelli Pl, Cambridge MA, 02138

<sup>†</sup>Contributed equally. \*Correspondence to [gsimpson@purdue.edu](mailto:gsimpson@purdue.edu)

### 1. QCL spectral channels characteristics and modulated pulse train profile

QCL Channel number	Spectral Peak(cm <sup>-1</sup> )	QCL Channel number	Spectral Peak(cm <sup>-1</sup> )
1	1339.34	17	1257.80
2	1333.98	18	1251.83
3	1328.67	19	1248.52
4	1323.19	20	1243.82
5	1318.01	21	1239.12
6	1312.88	22	1233.51
7	1306.01	23	1230.20
8	1302.58	24	1225.56
9	1297.21	25	1220.92
10	1290.77	26	1216.64
11	1285.76	27	1212.24
12	1282.51	28	1207.84
13	1277.21	29	1202.30
14	1270.94	30	1199.28
15	1267.50	31	1195.00
16	1262.86	32	1190.72

**Table S1.** QCL laser channel numbers and corresponding wavelengths, as reported by the laser manufacturer.

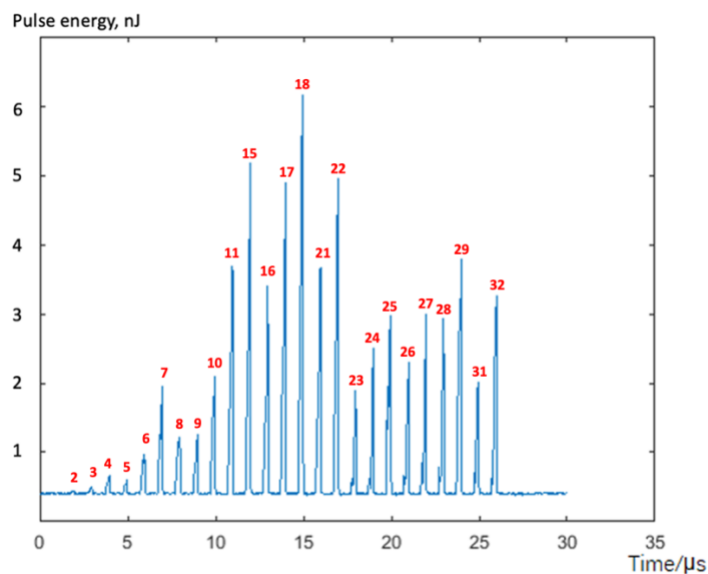


**Figure S1.** QCL pulse train profile (all channels driven by 16.5 V with 0.5  $\mu$ s delay, 300 ns pulses, channel numbers are shown in red). QCL channels 1, 12 – 14, 19-20 and 30 were not included in the pulse train, as they produced negligible power at the voltage setting used.

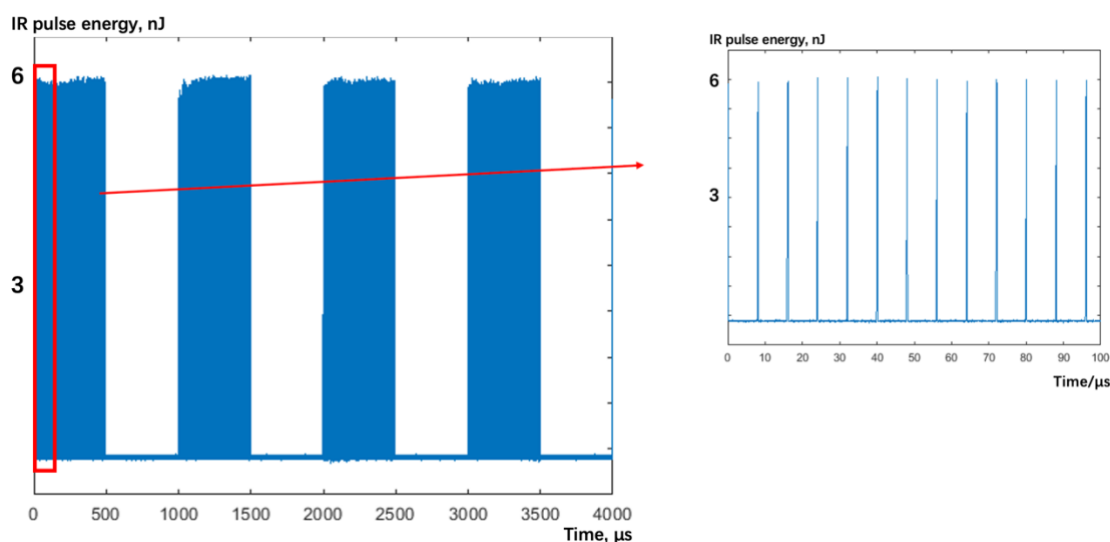


**Figure S2.** Modulated QCL pulse train profile (single channel mode). Spectral channel 18 is modulated at 1 kHz with 8  $\mu$ s delay between pulses.

## 2. F-PTIR Microscope quantitative characteristics

R6G-associated silica gel microscale particles were used as a sample to assess quantitative characteristics of the microscope setup. A single photon event produced a peak voltage recorded on an oscilloscope of  $\sim 100$  mV and an average voltage integrated over a 100 ns window of 0.055 mV. Upon fluorescence excitation with a 532 nm laser, the average integrated voltage over the same 100 ns window was 20 mV, which corresponds to approximately 364 single fluorescence photon-detection events in 100 ns or  $3.64 \times 10^9$  photons per second.

The modulation depth was calculated by comparing the modulated signal amplitude to the background fluorescence intensity collected in the absence of QCL operation (**Fig. S3**) The

modulation depth varied between different particles in the range between 1 and 5%, with an average modulation depth in locations producing F-PTIR response estimated to be 0.5-1%. Given the photon count calculated above, this corresponds to  $3.64 \times 10^7$  modulated photons per second or  $1.09 \times 10^6$  modulated photons per pixel within the 30 ms pixel dwell time. Therefore, the shot noise limit for our system at 1% modulation depth yields a theoretical maximum SNR based on Poisson statistics for 1% modulation of  $\sqrt{1.09 \times 10^6} = 740$ . In the main manuscript, silica gel samples produced signal-to-background ratio of 645 and signal to noise ratio of 300, with noise measured as the standard deviation of the fluorescence response in the absence of QCL modulation.

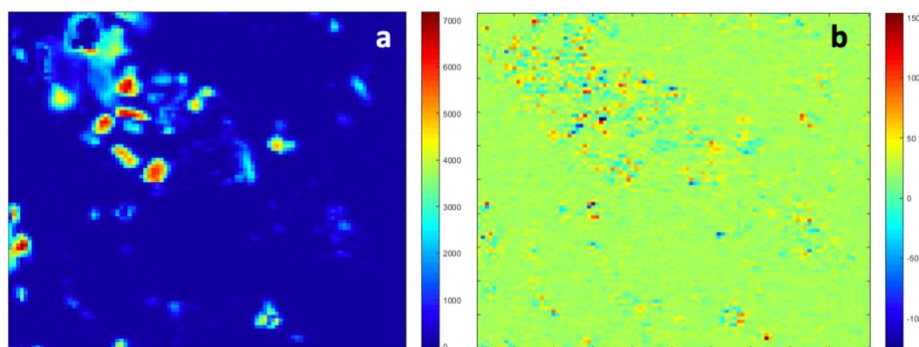


**Figure S3.** F-PTIR image collected with (a) and without (b) activating the QCL.

In order to demonstrate F-PTIR signal generation, the raw PMT readout was synchronized with the QCL reference output and digitized directly with the same digital oscilloscope cards used for image acquisition recorded (**Fig. S4**). The QCL pulse train was fired 8 times during the 0.5ms “on” period followed by a relaxation period of the same length. Each QCL reference signal represents a train of 32 pulses of 300ns width and 100ns gap between them. There is a clear reduction (positive voltage on the image means lower signal) in fluorescence intensity following each pulse train and a more general trend within the slower 1 kHz modulation window is also observed.

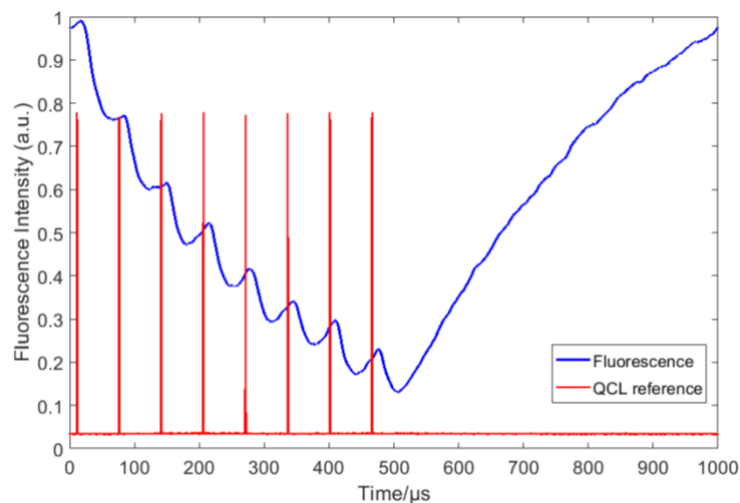


**Figure S4.** Mid-IR induced change in fluorescence intensity (blue). Red peaks correspond to the reference signal from the start of the QCL burst. Each reference pulse represents a 32-channel pulse train.

The spatial resolution of F-PTIR principle is limited by the resolution of the used fluorescence microscope. The resolution test of our system is illustrated in **Figure S5**. The size of one pixel was calculated based on the images of the clear-pass USAF test grid. We used the sharp edge analysis to calculate the resolution by taking a derivative of the signal intensity around the edge of a silica gel particle along the slow axis of the scan. The resolution of F-PTIR ( $1.7 \mu\text{m}$ ) approaches the resolution of the epi-fluorescence microscope ( $0.99 \mu\text{m}$ ), which indicates the possibility of performing super-resolution F-PTIR by integrating mid-IR lasers within super-resolution fluorescence microscopes.

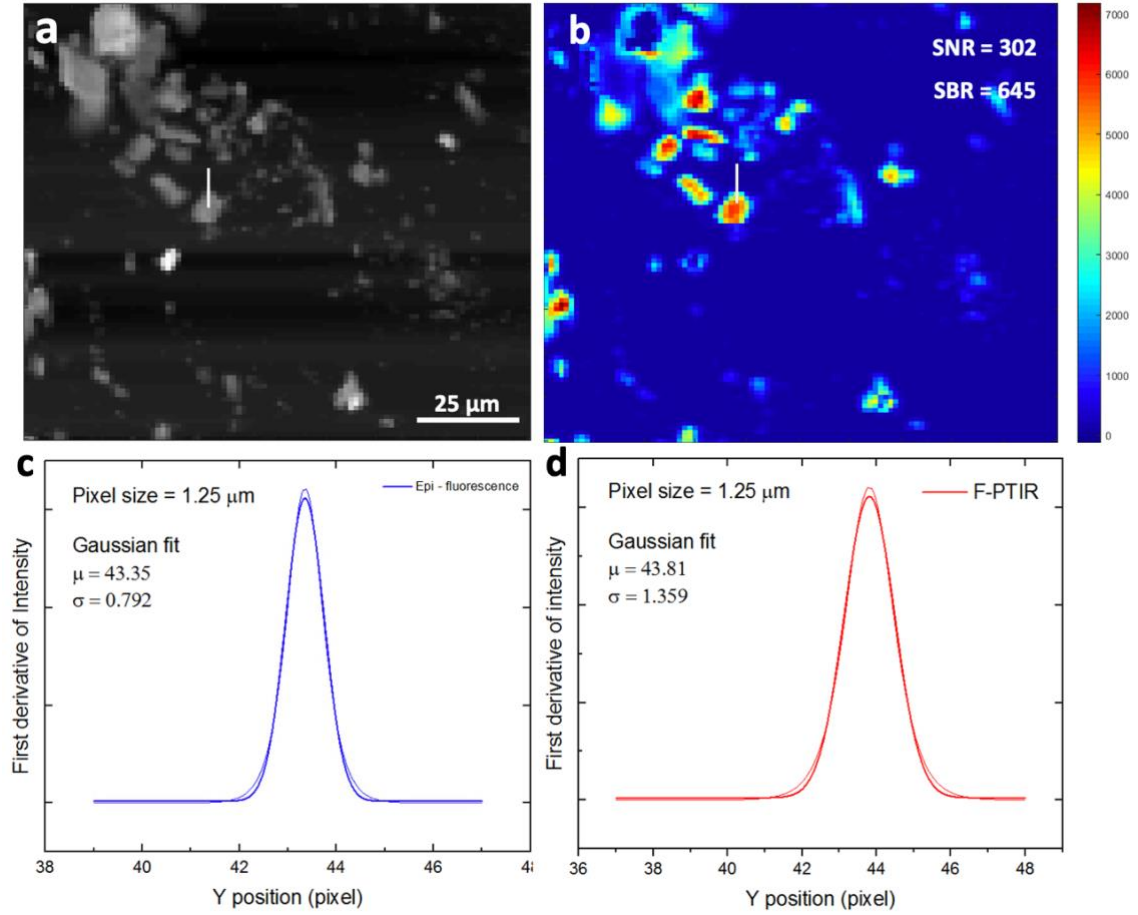


**Figure S5.** Resolution test of the F-PTIR microscope. (a) Epi-fluorescence image of the FOV. (b) Corresponding F-PTIR image. (c) and (d) First derivative of intensity profile along the vertical white lines in images a,b fitted to a Gaussian function.

### 3. F-PTIR microscope resolution

During the F-PTIR measurements, the QCL was modulated by an external function generator at frequencies up to 25 kHz, which corresponds to thermal diffusion length of  $1.54 \mu\text{m}$ . This length is comparable to the spatial resolution of the optical epi-fluorescence microscope used in the experiment (see above).

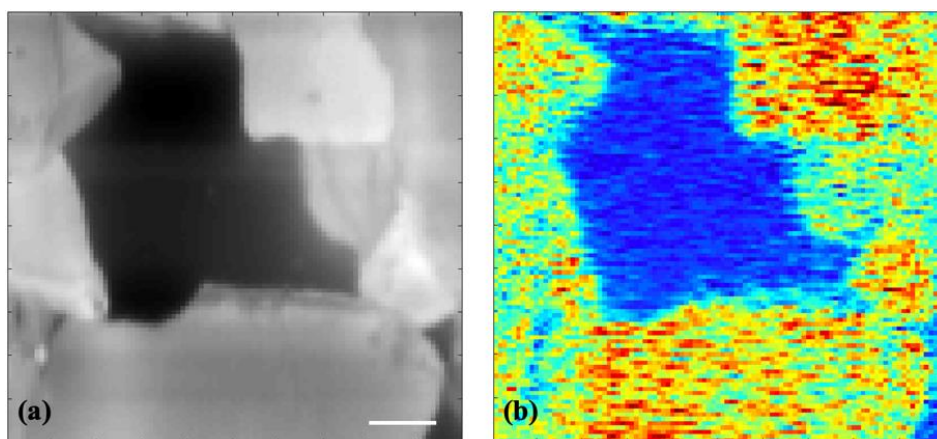


**Figure S6.** F-PTIR images of R6G-associated silica gel. (a) – epi-fluorescence field-of-view for reference. (b) – unprocessed F-PTIR image at 20 kHz modulation frequency, corresponding to a thermal diffusion length of 1.72  $\mu\text{m}$ . Scale bar is 10  $\mu\text{m}$ .

#### 4. Sample preparation

R6G- and fluorescein-associated solutions of solvents were prepared by dissolving 10 mg of rhodamine-6G (Sigma Aldrich) in 10 mL of solvent [deionized water, dimethylformamide (DMF, Sigma) and dimethyl sulfoxide (DMSO, Sigma)], corresponding to 2.1 mM concentration of R6G and 3 mM for fluorescein.

Due to high water content, silica gel (SG) exhibits strong absorption of IR radiation. Within the spectral range of our QCL, SG strongly absorbs at every wavelength channel without distinct spectral features, serving as a convenient model system for instrument testing. Polyethylene glycol (PEG), in contrast, has two sharp peaks within the QCL range (**Fig. 3** in the main manuscript), making it a suitable sample for testing spectral accuracy of the system.

R6G-associated silica gel particles were prepared by mixing 100 mg of silica gel (60-200  $\mu\text{m}$  particles, SiliCycle) and 5 mg of R6G in 10 mL of deionized water (1.05 mM R6G concentration) and air drying the extracted particles. R6G-associated polyethylene glycol (PEG) particles were prepared by air-drying a solution of 300 mg of PEG (Sigma Aldrich) and 10 mg of R6G in 10 mL of water (2.1 mM R6G concentration), from which smaller particles were recovered by grinding.

Thin films of ritonavir (RTV) associated polyvinyl pyrrolidone/vinyl acetate copolymer (PVP-VA) systems were prepared by spin-coating a stock solution of 300 mg/mL of 30% RTV (Sigma), 70% PVPVA (Sigma) and 0.1% Nile Red (Sigma) by weight in methanol. The films were left under vacuum overnight to remove residual solvent. Phase separation was induced by placing the thin films in the 100% relative humidity environment for 1 hour.

#### 5. Optical binary masks selection and non-negative matrix factorization

Binary classification between two components can, in principle, be performed with as few as two spectral measurements. However, statistical confidence improves through fully leveraging the discriminatory power of multiple spectral channels by operating the QCL in a

“burst” mode available using the Pendar QCL. Based on the IR spectra of pure components, activation of a small number of high SNR channels when designing the mask improved the minimized SNR degradation through the multiplex disadvantage (i.e., cross-talk between two signals from the two components). The final images shown in the manuscript (**Fig. 3**) were collected using two QCL channels in each mask exhibiting strong differences in IR absorption between the two components.

For further refinement of the spectral demixing, non-negative matrix factorization (NNMF) was used. For a two-component image measured using two optimized binary masks, the F-PTIR intensities in a given pixel can be written as a  $2 \times 1$  vector. The entire set of pairwise intensities can be represented by a  $2 \times N$  matrix  $\mathbf{D}$ , in which  $N$  is the number of pixels in the image.  $\mathbf{D}$  can be considered as the matrix product of the abovementioned binary masks  $\mathbf{M}$  by the matrix of QCL channels F-PTIR intensity in each image  $\mathbf{H}$  and concentration images of both components  $\mathbf{C}$ . The product of  $\mathbf{M}$  and  $\mathbf{H}$  is constant within one measurement, which is represented by a  $2 \times 2$  matrix  $\boldsymbol{\varepsilon}$ .

$$\mathbf{D}_{2 \times N} = \mathbf{M}_{2 \times 32} \times \mathbf{H}_{32 \times 2} \times \mathbf{C}_{2 \times N} \quad (\text{SI } 1)$$

$$\mathbf{D}_{2 \times N} = \boldsymbol{\varepsilon}_{2 \times 2} \cdot \mathbf{C}_{2 \times N} \quad (\text{SI } 2)$$

The concentrations of two components can be determined by inverting Eq. SI.2:

$$\mathbf{C} = (\boldsymbol{\varepsilon}^T \cdot \boldsymbol{\varepsilon})^{-1} \cdot \boldsymbol{\varepsilon}^T \cdot \mathbf{D} \quad (\text{SI } 3)$$

Uncertainty in the measured pure component spectra resulted in recovered values in  $\mathbf{C}$  less than zero, which is mathematically allowed but physically impossible. Similarly, the elements in  $\boldsymbol{\varepsilon}$  describing pure-component absorption are bound by physics to be positively valued. Iterative refinement in the pure component spectra and concentration maps was performed by NNMF using the following algorithm:

- (1) Replace any negative values in  $\mathbf{C}$  by 0 to generate new matrix  $\mathbf{C}_i$ , then solve for new  $\boldsymbol{\varepsilon}_i$

$$\boldsymbol{\varepsilon}_i = \mathbf{D} \mathbf{C}_i^T (\mathbf{C}_i \mathbf{C}_i^T)^{-1} \quad (\text{SI } 4)$$

- (2) Replace negative value in  $\boldsymbol{\varepsilon}_i$  by 0 to generate new  $\mathbf{C}_{i+1}$ .

- (3) Repeat steps 1 and 2 until there is no negative values in  $\mathbf{C}_{i+1}$ .

Unprocessed F-PTIR spectra of silica gel and PEG for the 25 most powerful QCL channels are shown in **Figure S7**. Spectral channels in the higher wavenumber region exhibit a stronger absorption for PEG, while channels starting with 17 were more strongly absorbed by SG. This case turned out to be relatively straightforward; the spectral masking algorithm assigned the first half of the channels as a first mask (PEG) and channels 16 - 32 as a second mask. However, strong absorption of silica gel at all available wavenumbers lead to some cross-talk between images. To minimize the interferences, we constructed masks based on only 2 channels for each component (**Fig. 3** in the main manuscript). The masks were subsequently optimized to maximize unmixing of the F-PTIR signal between species.

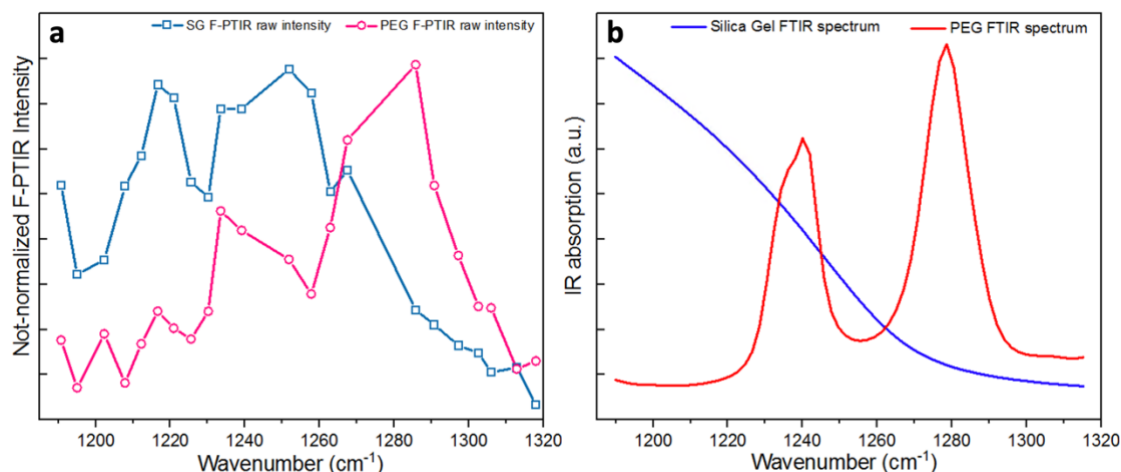


**Figure S7.** F-PTIR spectra of pure SG and PEG (not normalized to IR power).

## 6. Data processing for PVPVA – ritonavir phase separated samples

Though the general shape of the FTIR spectra for both components is similar (**Fig. S8**), features in the long-wavenumber region allowed the discrimination between components using the NNMF approach described above. The most apparent difference between components' spectra is around the peak at 1285 cm<sup>-1</sup> in PVPVA spectrum that is absent for ritonavir. As can be seen in **Fig S8C**, this feature was preserved in F-PTIR measurements for pure PVPVA and absent in the spectra for both pure ritonavir and bright region of the sample later assigned as ritonavir-rich by independent F-PTIR and TPE-UVF measurements (see main manuscript).

Due to the low film thickness, to avoid uncertainties associated with low SNR at some QCL low-intensity spectral channels (see **Fig. S1**), F-PTIR intensity of pure components and the phase-separated sample were acquired at every accessible QCL channel prior to generating the spectral masks. Afterwards, the NNMF iterative optimization was performed as described in section 5.

To increase the assignment accuracy and signal to noise ratio, unprocessed F-PTIR images of RTV-PVPVA samples were first divided into 27 larger regions (superpixels). The algorithm calculated mean intensity value for each superpixel and the subsequent analysis was done on a superpixel-by-superpixel basis (compared to pixel-by-pixel analysis for the model silica gel – PEG system). The segmentation was done by using the superpixel oversegmentation approach described in [2]. Then, the same approach as described in (6) was applied to calculate the concentrations of components. Each superpixel was assigned to either ritonavir, PVPVA or background.



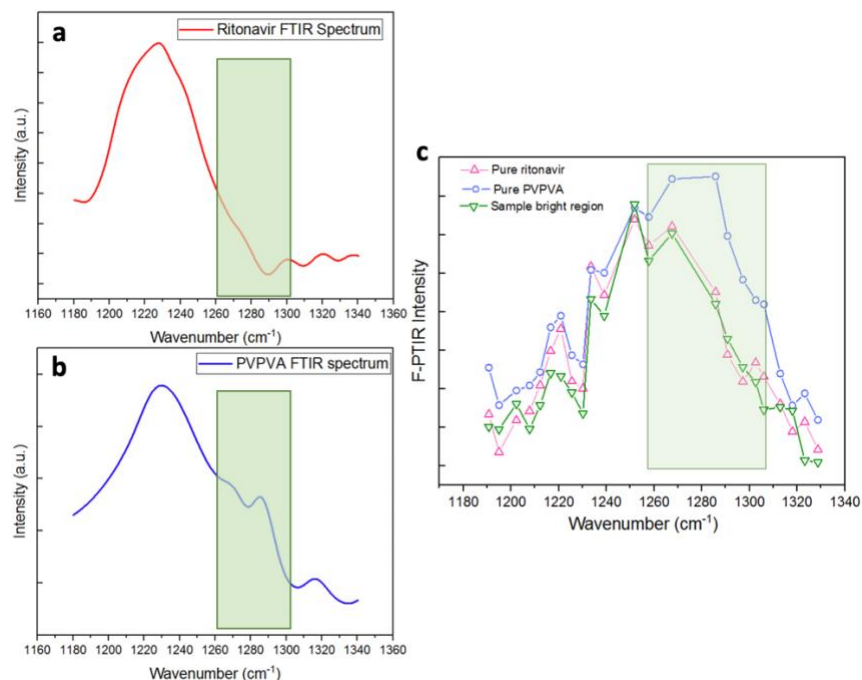


**Fig. S8.** FTIR spectra of ritonavir (a) and PVPVA (b). (c) – Unprocessed (not normalized) F-PTIR intensity for pure components and the bright region of the amorphous film. Green box highlights the spectral region used for NNMF discrimination.

## 7. FRAP analysis of diffusivity within phase-separated domains.

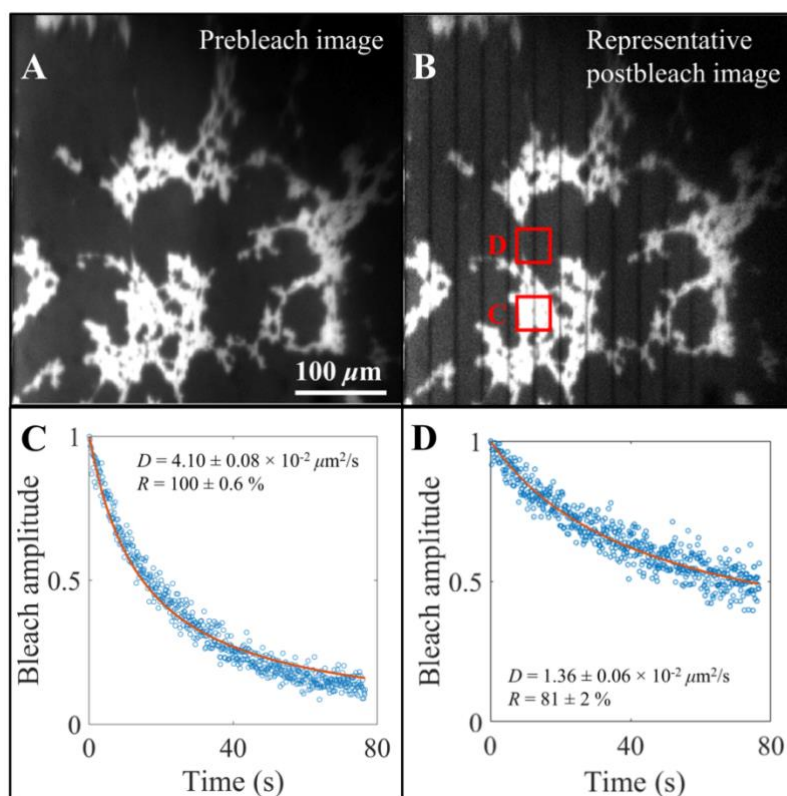


**Figure S9.** Fluorescence recovery after photobleaching measurements within the two phase-separated regimes. Diffusion coefficients recovered within the different regimes exhibited marked differences.

Fluorescence recovery after photobleaching with patterned illumination was performed to assess Nile Red fluorescence mobility within the different phase-separated regimes, the



results of which are summarized in **Figure S9**. In brief, illumination with a comb photobleach pattern produced stripes within the field of view. A one-dimensional diffusion model was used to interpret the recovery as a convolution of the initial bleach profile  $C(x,0)$  with a time-varying Gaussian distribution with a variance of  $2Dt$  as the solution to the diffusion equation as described below, in which  $D$  is the isotropic diffusion coefficient and  $t$  is time.

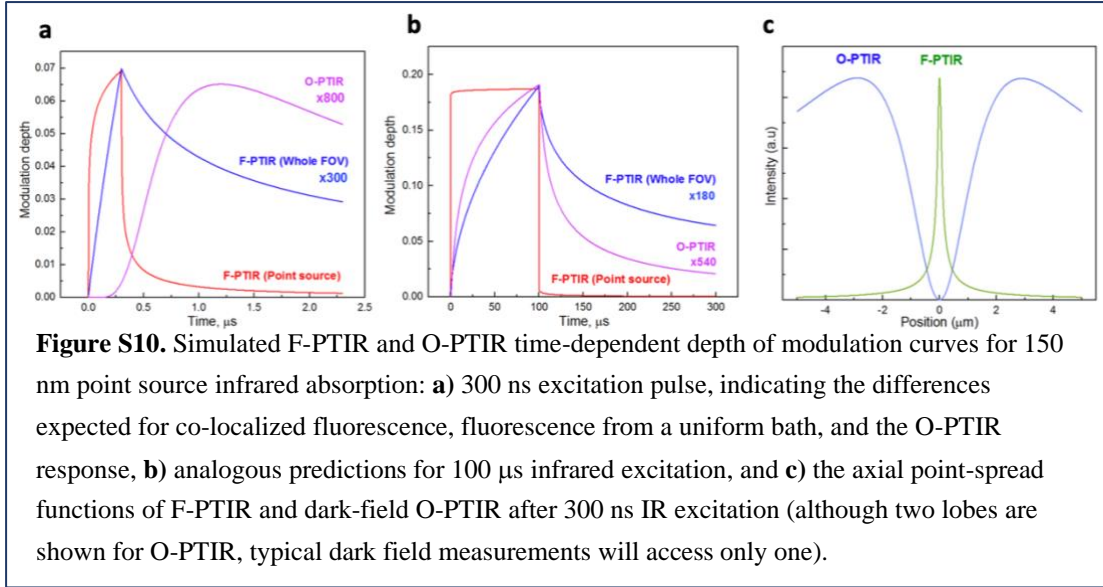
$$C(x,t) = C(x,0) \otimes \frac{1}{\sqrt{2\pi\sigma_t^2}} e^{-\frac{x^2}{2\sigma_t^2}}; \sigma_t^2 = 2Dt \quad (\text{SI } 5)$$

Cross-sections within the boxed regions in **Figure S9.B** were fit to Equation SI.5 at each time-point after the photobleach. The amplitudes of the time-varying Gaussian functions were then plotted as a function of time, the results of which were then fit to recover the diffusion coefficients  $D$  indicated in **Figures S9.C** and **S9.D**. The fits also included the recoverable mobile fraction  $R$ , which were close to unity for both domains. The recovered diffusion coefficients of Nile Red differed by a factor of  $\sim 3$ , demonstrating clear differences in local viscosity within the different phase-separated domains.

## 8. F-PTIR Simulations

Custom simulation software for modeling the F-PTIR response from a nanoscale point-source was written in MATLAB to evaluate the anticipated time-dependent point spread function. Beam parameters for fluorescence excitation were based on the assumption of Gaussian beam profiles for an NA of 0.3, a fluorescence excitation wavelength of 532 nm, and an infrared wavelength of  $\sim 10 \mu\text{m}$ , consistent with the experimental measurements.<sup>8</sup> F-PTIR simulations were performed for 150 nm “point source” particles, with either 300 ns or 100  $\mu\text{s}$  IR excitation pulses with heat production localized to the point source, using the thermal diffusivity of room temperature water ( $143 \text{ nm}^2/\text{ns}$ ). From the simulated spatiotemporal temperature distribution during both the photothermal activation and subsequent relaxation upon cessation of the infrared excitation, the change in fluorescence was considered in two limiting cases: i) colocalization of fluorescence within the PTIR absorbing source (assumed to be colocalized within a 150 nm radius), and ii) isotropic fluorescence within the focal volume but not co-localized with the PTIR excitation.

The results of the simulations are shown in **Figure S10**, revealing interesting trends. In the case of colocalization for a single 300 ns IR pulse, the temperature change and corresponding F-PTIR response exhibits a bimodal trend, with rapid heating within the initial pulse onset until steady-state is achieved between point-source heat deposition and heat dissipation. Following cessation of the IR excitation, the change in fluorescence within the colocalized nanoscale region of interest rapidly ( $\sim 100 \text{ ns}$ ) decays and approaches the much lower baseline change in fluorescence approaching the change in temperature within the entire focal volume. These trends are in stark difference to the anticipated F-PTIR response expected for isotropic fluorescence within the bath rather than colocalized, in which the peak change in fluorescence is  $\sim 100$ -fold less than that of the co-localized nanoparticle response and orders of magnitude slower in the thermal relaxation time. These trends are remarkably consistent for both short (300 ns) and long (100  $\mu\text{s}$ ) pulsed infrared excitation, with the steady-state plateau more prominent for the longer pulse duration.



These collective results suggest substantial potential signal to noise advantages in F-PTIR in samples in which the fluorophore is selectively co-located within the regions of infrared absorption. These advantages arise through both signal increases and noise suppression. Signal is expected to increase by positioning the fluorophores at locations with the greatest temperature changes induced by IR absorption. Average temperatures following diffusion throughout the entire focal volume are much lower than the peak temperatures realized at positions immediately adjacent to the IR absorbing source. Noise suppression arises in co-localization by reducing shot (Poisson) noise from fluorophores within the bath exhibiting negligible modulation.

Anticipated trends for the corresponding O-PTIR response were also evaluated based on a model developed by Cichos and coworkers for a Gaussian probe beam and a nanoparticulate source.<sup>3</sup> The model approximates the O-PTIR response based on a thermal gradient index lens, which was found to accurately recover the O-PTIR point spread function measured for 60 nm Au nanoparticles. The effective focal length of the photothermal lens is given by the following expression.

$$f_{\text{eff}}(z_p) \cong \frac{n}{\Delta n} \frac{W_0^2}{4R} \left[ \frac{z_p^2}{Z_0^2} + 1 \right] \quad (\text{SI.6})$$

In Equation SI.6,  $\Delta n$  is the change in refractive index induced by local photothermal heating,  $W_0$  describes the radial beam waist for a Gaussian probe beam,  $Z_0$  is the Rayleigh range defining the axial extent of a Gaussian beam,  $R$  is the particle radius, and  $n$  is the refractive index of the surrounding medium (assumed to be 1.33 for water in the simulations).

Consistent with the prior measurements/modeling by Cichos and coworkers, the point spread function (PSF) for photothermal microscopy exhibits a node of zero amplitude for a point source centered within the probe beam focal plane and is markedly different from a conventional Gaussian beam PSF expected for F-PTIR. Furthermore, the maximum in the PSF for O-PTIR is axially offset from the focal plane of the probe beam, such that bright-field/fluorescence and O-PTIR signals generally do not probe the same sample plane. In a dark-field O-PTIR configurations based on detection of beam deflection, only one of the two

lobes shown in **Figure S10.c.** will generally be experimentally accessible, leading to large axial asymmetry in the PSF not present in F-PTIR. The much larger predicted axial extent of the PSF in O-PTIR relative to F-PTIR is a consequence of diffuse infrared excitation from the longer assumed wavelength ( $\sim 10\ \mu\text{m}$  in these simulations) together with increases in beam deflection from geometric optics as the thermal lens is displaced away from the focal volume. Finally, dark field configurations commonly used in O-PTIR inherently exhibit higher detected light flux from locations of scatter/refraction, including interfaces within the sample. If the O-PTIR signals is not rescaled by the average detected intensity measured at that location, the higher flux in dark-field O-PTIR can increase the amplitude of modulation proportionally. The corresponding increase in O-PTIR modulation amplitude arising from scattering in dark-field geometries has the potential to bias the interpretation of image contrast if attributed to IR absorption alone. The interplay between scattering within the probe beam focal plane and O-PTIR within an offset focal plane may produce nontrivial image contrast in dark-field O-PTIR microscopy. Such sources of bias from scattering were not incorporated in the O-PTIR simulations.

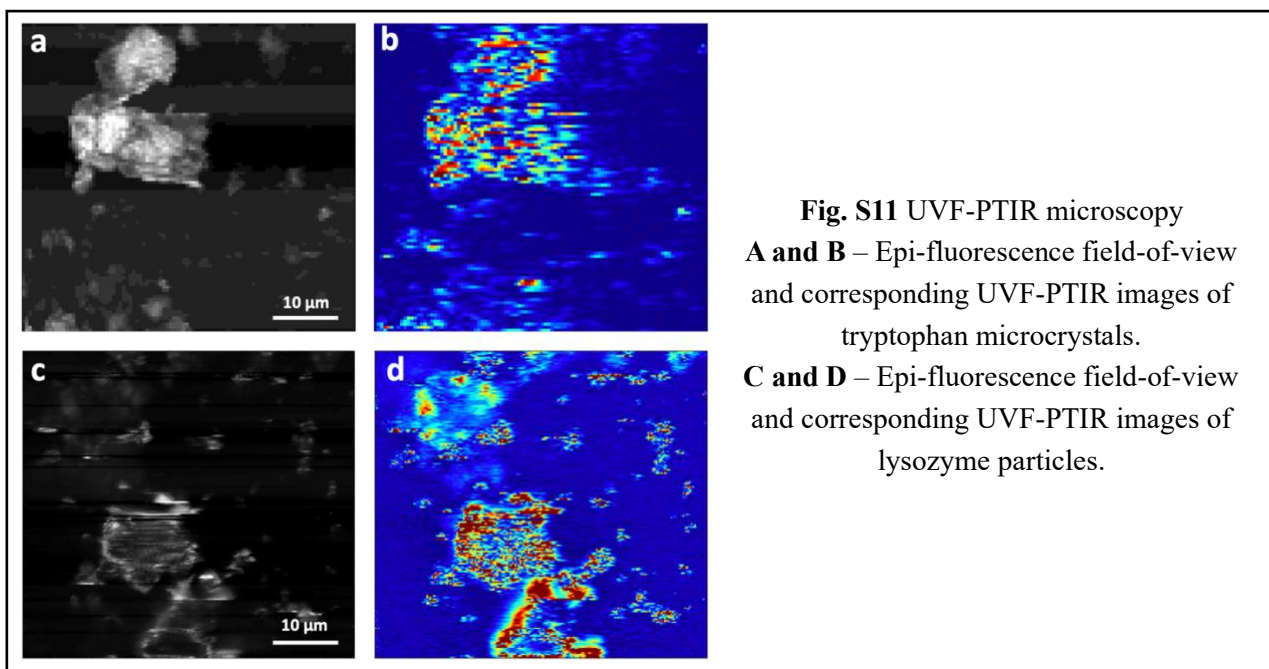
Simulations of the time-dependent and position-dependent O-PTIR response are shown in **Figure S10.** The O-PTIR response was assumed to be proportional to the change in beam position at the maximum NA of the objective, representing an upper bound for the sensitivity of a dark-field measurement configuration. The temperature change used to calculate the effective focal length was evaluated by considering the temperature at an offset of  $W_0$  relative to the point source center position and setting  $\Delta n$  equal to the maximum of a corresponding Gaussian temperature distribution centered on the point source for compatibility with the Gaussian beam propagation expressions from Cichos and coworkers.<sup>3</sup> Since the O-PTIR signal is zero for a point source positioned at the focal point of the probe beam, the point source was assumed to be axially offset by a displacement of  $\sqrt{3}Z_0$ , which yields the theoretical maximum sensitivity.<sup>4,5</sup> All source code for F-PTIR and O-PTIR simulations is archived and available at <https://github.itap.purdue.edu/Simpson-Laboratory-for-Nonlinear-Optics/FPTIR.git>.

From the simulations, the O-PTIR response exhibits several interesting trends relative to F-PTIR. First, as expected, simulations of the O-PTIR response as a function of axial position in **Figure S10.c** indicate a node in the signal for a photothermal point source positioned in the focal plane of the probe beam, with maximum sensitivity offset by displacements of either  $\pm\sqrt{3}Z_0$  (typical dark-field configurations will exhibit sensitivity to either positive or negative displacement, but not both). These predictions are consistent with experimental measurements and modeling of photothermal microscopy of isolated nanoparticles by Cichos and coworkers.<sup>3</sup> In contrast, the F-PTIR sensitivity is expected to scale directly with the intensity distribution within the excitation beam (also shown in **Figure S10.c.** for reference). Assuming a probe beam offset of  $\sqrt{3}Z_0$ , the time-dependent evolution of the O-PTIR response maps closely that of the F-PTIR signal expected for fluorescence from an isotropic bath. In retrospect, this result is consistent with both O-PTIR and non-localized F-PTIR producing signals scaling with the net temperature change across the entire focal volume, while localized F-PTIR produces much faster response times following excitation and cessation. Finally, the maximum relative change in the O-PTIR response is several orders of

magnitude smaller than either model for F-PTIR, consistent with the small expected change in refractive index with temperature compared to that of fluorescence.

### 9. Label-Free UVF-PTIR Intrinsic Autofluorescence Measurements

Two-photon excitation supported label-free F-PTIR microscopy. Most proteins exhibit native UV-fluorescence activity excitable by two-photon absorption with  $\sim 100$  fs pulses of 532 nm light due to the content of aromatic amino acids residues, mainly tryptophan with an emission peak centered around 350 nm.<sup>6</sup> TPE-UVF is also natively observed in many small molecule active pharmaceutical ingredients.<sup>7</sup> Autofluorescence of proteins can also be excited by nonlinear two-photon absorption when using ultrafast excitation visible source. Proof-of-concepts measurements of label-free fluorescence-detected mid-infrared photothermal microscopy in the UV-region (UVF-PTIR) are shown in **Figure S11**. Measurements were obtained using an ultrafast Nd-YAG laser source (NKT Photonics Fianium FemtoPower 1060) frequency-doubled to 532 nm. Initial measurements performed using pure tryptophan microcrystalline powder (Sigma, 98%) showed good agreement between the recovered UVF-PTIR and FTIR spectra (**Fig. 2D** in the main manuscript). Building on these results, images of lyophilized lysozyme particles (Sigma, lysozyme from chicken egg white) shown in **Fig. S11 C,D** demonstrate high UVF-PTIR contrast for protein-rich locations. In the wavelength regime accessible by the current QCL laser source, the infrared absorptivity of lysozyme was featureless and is not included.



### References:

- [1] – H. Shimizu, K. Mawatari, T. Kitamori *Anal. Chem.* **2010**, 82, 7479–7484
- [2] – Radhakrishna Achanta, Appu Shaji, Kevin Smith, Aurelien Lucchi, Pascal Fua, and Sabine Susstrunk, SLIC Superpixels Compared to State-of-the-art Superpixel Methods. *IEEE Transactions on Pattern Analysis and Machine Intelligence*, Volume 34, Issue 11, pp. 2274-2282, May **2012**
- [3] – Markus Selmke, Marco Braun, and Frank Cichos, Gaussian beam photothermal single

particle microscopy, *J. Opt. Soc. Am. A*, Vol. 29, Is. 10, p. 2237, **2012**.

[4] Hawkes, J. B.; Astheimer, R. W., The Temperature Coefficient of the Refractive Index of Water. *Journal of the Optical Society of America* **1948**, 38 (9), 804-806.

[5] Tokeshi, M.; Uchida, M.; Hibara, A.; Sawada, T.; Kitamori, T., Determination of Subyoctomole Amounts of Nonfluorescent Molecules Using a Thermal Lens Microscope: Subsingle-Molecule Determination. *Analytical Chemistry* **2001**, 73 (9), 2112-2116.

[6] Madden, J. T.; DeWalt, E. L.; Simpson, G. J. "Two-Photon Excited UV-Fluorescence for Protein Crystal Detection" *Acta Cryst. D* **2011**, D67, 839-846.

[7] Toth, S.J.; Schmitt, P.D.; Snyder, G.R.; Trasi, N.J.; Sullivan, S.Z.; George, I.A.; Taylor, L.S.; Simpson, G.J. "Ab Initio Prediction of the Diversity of Second Harmonic Generation from Pharmaceutically Relevant Materials." *Crys. Growth and Des.* **2015**, 15, 581–586.

[8] Saleh, Bahaa E. A., and Malvin Carl Teich. *Fundamentals of Photonics*. New York: Wiley, 1991.